Chapter 1

Theoretical Study of Superconductivity in 4-Angstrom Carbon Nanotube Arrays

Ting Zhang, Mingyuan Sun, Zhe Wang, Wu Shi, Rolf Lortz, Zikang Tang, Ning Wang, and Ping Sheng

Department of Physics and William Mong Institute of Nano Science and Technology, Hong Kong University of Science and Technology, Clear Water Bay, Kowloon, Hong Kong, China

sheng@ust.hk

We review the recent theoretical progress in understanding the superconductivity observed in ultrathin 4-Angstrom carbon nanotubes (CNTs) embedded in the linear channels of the aluminophosphate-five ($AlPO_4$–5, AFI) zeolite crystals. To identify the ground state of the (5,0) CNT@AFI system, we have carried out second-order renormalization group (RG) analysis to show that if arranged in an array structure in the channels of an AFI crystal, superconductivity can dominate over the Peierls distortion mechanism to be the favored state. However, if the array is very thin, then the manifestation would be that of one-dimensional (1D) superconductivity, displaying finite resistance at finite temperatures. We give a brief description of the phase slip mechanism underlying this behavior. With transverse Josephson coupling between the (5,0) CNT arrays, a 1D to three-dimensional (3D) crossover transition

Carbon-Based Superconductors: Toward High-Tc Superconductivity
Edited by Junji Haruyama

ISBN 978-981-4303-30-9 (Hardcover), 978-981-4303-31-6 (eBook)
www.panstanford.com

can occur at a temperature below which 3D superconducting behaviors appear. By carrying out Monte Carlo (MC) simulations on a transversely discretized Ginzburg–Landau (GL) model, we show that both the thermal specific heat and electrical data can be well explained. In particular, just above the dimensional crossover transition, the phase correlation function exhibits the signature of a Berezinskii–Kosterlitz–Thouless transition in good agreement with the measured temperature dependence of resistance.

1.1 Introduction

Since the first observation of superconductivity in ultrathin carbon nanotubes (CNTs) embedded in AFI zeolite crystals [1], there has been much experimental and theoretical works devoted to this subject. In this chapter, we summarize the recent progress in the theoretical analysis of superconductivity in 4-Angstrom CNT arrays. The paper is organized as follows. Section 1.2 gives a brief introductory description of the relevant material system. Section 1.3 is devoted to the RG analysis of such CNT@AFI system, aimed at identifying the zero temperature ground state between two competing mechanisms—superconductivity and the Peierls distortion (the charge density wave, or CDW) state. In Section 1.4, we give a short review on the origin of electrical resistance in 1D superconductors, based on the physical picture of phase slips as mathematically formulated by the Langer–Ambegaokar–McCumber–Halperin theory. In Section 1.5, we use Monte Carlo simulation of the Ginzburg–Landau model to explain the specific heat and electronic transport characteristics in the (1D to 3D) dimensional crossover transition, leading to the observed 3D superconductivity. We conclude in Section 1.6 with an overview summary of the salient points.

1.2 The CNT@AFI System

CNTs were first grown inside the channels of porous AFI zeolite with pyrolysis of the precursor molecules—tripropylamine [2]. AFI is a micro-porous zeolite crystal with aligned linear channels. The channels are hexagonally close packed in the transverse a–b plane, each with an inner diameter of 7.3 Å and separated by a

center to center distance of 13.7 Å. Inside the channels, a fraction of the carbon atoms, from the pyrolysis of tripropylamine precursor, formed single-wall carbon nanotubes that are ~4 Å in diameter. This is confirmed by high-resolution transmission electron microscopy observation [2], adsorption spectra [3], and Raman spectra [4–6], in which the characteristic radial breathing mode, particular to the tube structure, was observed. A sketch of the AFI zeolite with embedded CNTs is shown in Fig. 1.1.

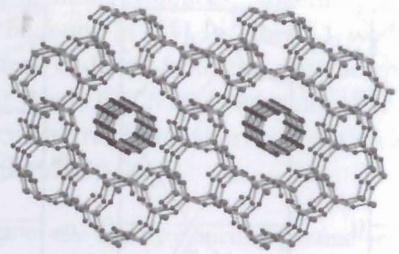

Figure 1.1 A schematic picture illustrating the structure of AFI zeolite with embedded 4-Angstrom carbon nanotubes. The lattice constant is 13.7 Å, and the pore diameter is 7.3 Å.

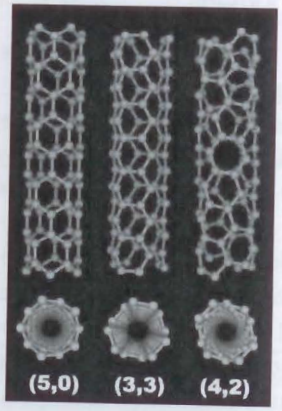

Figure 1.2 The three possible 4-Angstrom carbon nanotubes with the chiral indices of (5,0), (3,3), and (4,2). Adapted from Ref. [4].

Owing to the diameter of AFI channels, only three CNTs with diameter around 4 Å are possible: the armchair (3,3) (d ~ 3.9 Å), the zigzag (5,0) (d ~ 4.0 Å), and the chiral (4,2) (d ~ 4.1 Å). Their structures are shown in Fig. 1.2. Many authors have performed band structure calculations of these three types of CNTs [3,4,7–10].

The armchair (3,3) nanotube is metallic, and the chiral (4,2) nanotube is semiconducting, as expected. However, for the zigzag (5,0) nanotube, the prediction of the zone-folding scheme is not valid, owing to the mixing of the σ and π bonds that results from the large curvature effect. The net result is that the (5,0) nanotube is metallic. The local density approximation (LDA) band structures of these three CNTs are shown in Fig. 1.3. Superconductivity observed in this system is attributed to the (5,0) CNTs.

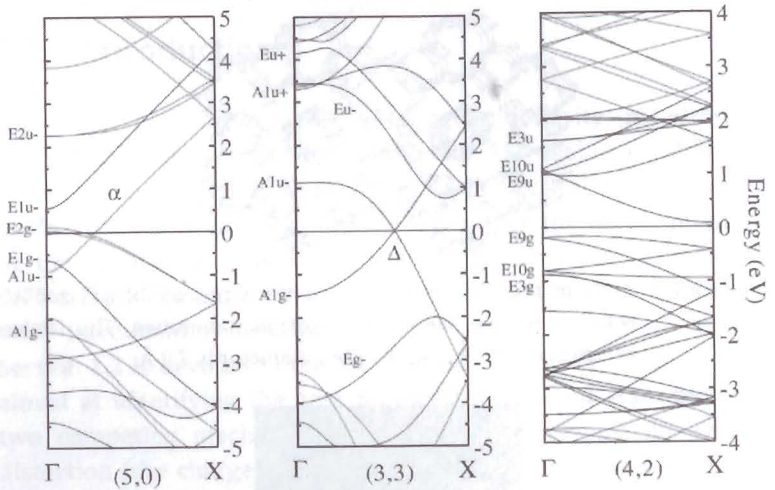

Figure 1.3 The LDA band structures of the three 4-Angstrom CNTs. The zigzag (5,0) and the armchair (3,3) are metallic, while the chiral (4,2) is semiconducting. Adapted from Ref. [4].

The seminal work of the Berkeley group has shown that the electron–phonon interaction can increase dramatically with decreasing radius [11]. Hence, the physical process that is related to the electron–phonon interaction, such as the phonon-mediated superconductivity, can occur in CNTs, especially when the radius is small. However, the electron–phonon interaction can also induce Peierls distortion in (3,3) and (5,0) CNTs that would lead to a semiconducting ground state [12–17]. There has been a persistent debate about which one should be the ground state of these small-radius CNTs, in spite of the experimental observations of superconductivity in the CNT@AFI system. This debate has motivated our RG work, presented in the following section. The outcome of our analysis is that whereas Peierls distortion would win over

superconductivity for a single (5,0) CNT, the situation is reversed for the (5,0) nanotubes when they appear in the form of tightly bundled arrays. Here the crucial element is the dielectric screening, absent for a single CNT, which can reduce the electron–electron interaction and thereby enhance the superconductivity.

Recently, the Meissner state [18], the electrical superconducting transition [19], and the superconducting thermal specific heat anomaly [20] were observed in the 4-Angstrom CNT@AFI. A review of these experimental evidences, together with a coherent description, can be found in [21]. In Table 1.1, we list the superconducting parameters deduced from the different measurements. It can be seen that the (5,0) CNT@AFI system is an extreme type II superconductor, with a relatively short correlation length and an H_{c1} that is on the order of 100 G.

Table 1.1 Values of the superconducting parameters as deduced from different measurements

	Transport measurement	**Magnetic measurement**	**Specific heat measurement**
T_C^0	15 K	15~18 K	14~18 K (exp.) 15 K (best fit)
T_C	6.2 K	6~7 K	–
H_{C1} for the Meissner state	–	~60 to 150 Oe	~100 ± 50 Oe
H_{C2} for the 3D coherent state	$H_{C2\perp} = 1.5$~5 T $H_{C2//} = 5$~13 T	$H_{C2\perp} \approx 1$ T	$H_{C2\perp} \approx 2.8$ T
ξ_0	ξ_{ab} ~ 5 to 8 nm ξ_c ~ 6.6 to 12 nm	~18 nm	14 ± 2 nm
λ	–	~1.4 μm	1.5 ± 0.7 μm
κ	–	~78	~110

Note: T_C^0 is the critical temperature that Cooper condensation begins to form along the *c*-axis. Below this temperature, the 1D fluctuation superconductivity is observed. T_C is the 1D to 3D crossover transition temperature, below which the 3D coherent superconductivity behavior occurs via BKT-like transition in the *a*–*b* plane that is transverse to the *c*-axis of the CNTs. H_{C1} is the lower critical magnetic field, and H_{C2} is the upper critical magnetic field at which the 3D superconductivity is suppressed. ξ_0 is the zero-temperature coherence length. λ is the magnetic penetration length, which is very large because of the porous nature of the system. The Ginzburg-Landau κ~100 is the ratio between λ and ξ_0, which indicates our CNT@AFI system to be an extreme type II superconductor. Adapted from Ref. [21].

The observation of 3D superconducting behavior also presents another problem, in view of the Hohenberg–Mermin–Wagner theorem [22,23], which states that there can not be a sharp

phase transition in dimension $d \leq 2$. Here, the small wall-to-wall separation between the nanotubes, only 9.7 Å as stipulated by the nanogeometry of the AFI zeolite, turns out to be important in enabling the Josephson coupling between the neighboring nanotubes. Indeed, simulations based on weak inter-tube Josephson coupling has shown a 1D to 3D crossover transition to be inevitable (Section 1.5), with all the attendant characteristics as observed experimentally.

1.3 RG Treatment of Ultrathin (5,0) CNT Arrays

The ground state of a 1D electronic system is usually regarded as a Luttinger liquid, which can be shown exactly through the bosonization method [24–31]. However, the Luttinger liquid model is based on the fact that there is no attractive interaction between the electrons. Since the problem of superconductivity inherently involves electron pairing that results from the attractive interaction, we have to go beyond the Luttinger liquid model and carry out the RG calculations to the second order. This is the focus of this section.

The RG method is very powerful in handling 1D interacting fermions [32–38]. In 1D fermion systems, the Feynman diagrams yield divergent integrals, which is hard to handle with the perturbative method. With the RG method, we can handle such divergent integrals and calculate and compare the different response functions, as well as the interacting coupling constants, with decreasing temperature. With this process, the coupling constants scale to the so-called fixed points. We can evaluate the ground state of a certain system with these fixed point values of the coupling constants. The Luttinger liquid represents just the fix point obtained from repulsive coupling, with backward-scattering scaling to zero under this condition. Here, we summarize the method of RG treatment for the single (5,0) nanotube and a thin array of (5,0) nanotubes [39–41]. The latter is meant to correspond with the experimental system. There is an extensive literature on the RG method [32–38] as applied to 1D electronic systems. Here, we emphasize the physical descriptions and those aspects that are special to our treatment. Mathematical details can be found in the references.

1.3.1 Linearization of (5,0) CNT Band and Definition of Coupling Constants

As seen in Fig. 1.3, for the (5,0) nanotube, there are three bands crossing the Fermi energy. One is denoted by B band with $\pm k_{FB}$ as Fermi points, while the other two bands are degenerate in energy and denoted as A and A′, respectively. They have Fermi points $\pm k_{FA}$ with $k_{FA} < k_{FB}$, and Fermi velocities $|v_{FA}| < |v_{FB}|$. As we are interested in the low-temperature properties of the system, only the states near the Fermi level are important. They are inside a narrow range $[E_F - E_c, E_F + E_c]$. Here, E_c is the energy cutoff. In one dimension, there is an equivalent expression of the previous statement: only the states with momentum near the "Fermi points" $\pm k_{FA'}$ $\pm k_{FB}$ are important and need to be considered, which are in the range $\{[-k_{FA} - k_{c'} - k_{FA} + k_c], [k_{FA} - k_{c'} k_{FA} + k_c]\}$ and $\{[-k_{FB} - k_{c'} - k_{FB} + k_c], [k_{FB} - k_{c'} k_{FB} + k_c]\}$. Within this region, the curvature of the energy dispersion curve is negligible. The linearized energy dispersion around Fermi energy is shown in Fig. 1.4(a), and the corresponding non-interacting Hamiltonian can be expressed as

$$H_0 = \sum_{\alpha=\uparrow\downarrow} \sum_{m=A,A',B} \sum_{k} \left(\varepsilon_{k_F m} a^+_{km\alpha} a_{km\alpha} + \varepsilon_{-k_F m} b^+_{km\alpha} b_{km\alpha} \right) \tag{1.1}$$

with $$\varepsilon_{k_{FA}} = \varepsilon_{k_{FA'}} = \begin{cases} -v_{FA}(k - k_{FA}) & k \sim k_{FA} \\ v_{FA}(k + k_{FA}) & k \sim -k_{FA} \end{cases}$$ and

$$\varepsilon_{k_{FB}} = \begin{cases} -v_{FB}(k - k_{FB}) & k \sim k_{FB} \\ v_{FB}(k + k_{FB}) & k \sim -k_{FB} \end{cases},$$

where a^+ and a are the creation and annihilation operators of electrons for states near k_{FA} and k_{FB}, respectively, while b^+ and b are the creation and annihilation operators for $-k_{FA}$ and $-k_{FB}$, respectively. The symbol α denotes the spin index. In Fig. 1.4(b), the Brillouin zone (BZ) of the (5,0) CNT is shown as the cutting line in the 2D graphene BZ. Since the CNTs can be regarded as rolling up of a 2D graphene sheet, the additional periodic boundary condition perpendicular to tube axis is imposed in the 2D graphene BZ. Therefore, only the states that fall on the cutting lines will survive, as shown in Fig. 1.4(b). The three cutting lines connecting A– and A+, B– and B+, as well as A′– and A′+ are associated with the energy dispersion lines crossing the

Fermi energy in the band structure. The six points A±, B±, and A′± denote the corresponding Fermi points.

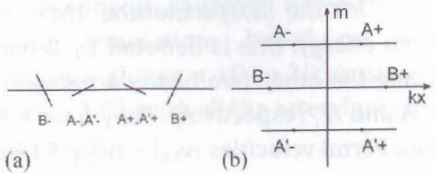

Figure 1.4 (a) The linearized energy dispersion of (5,0) CNT around the Fermi energy. The A and A′ bands are degenerate in energy, with opposite group velocity compared with the B band. (b) The cutting lines in graphene's 2d BZ, which are the permitted states with periodic condition around nanotube's circumference direction.

Figure 1.5 The three types of interactions. (a) Spin parallel backward scattering-process with the coupling constant $g_{1//}$. (b) Spin antiparallel backward-scattering process with the coupling constant $g_{1\perp}$. (c) Forward-scattering process with the coupling constant g_2.

Consider the interaction between the electrons. Since the Fermi energy E_f is not located at the half-filling level, Umklapp interaction is negligible. We are interested in processes in which the two associated electrons are such that one is left-moving and the other is right-moving. In such a scattering process, the perturbation expansion integral is divergent as $\log(\omega/E_C)$, where the energy scale ω can be regarded as temperature. By considering momentum conservation, for each combination of two bands with opposite Fermi velocities, there are three different types of electron–electron interactions that are important in the RG analysis, shown

in Fig. 1.5. These coupling constants are denoted as $g_{1//}$, $g_{1\perp}$, and g_2, as specified in the figure. For the g_1-type process, one electron scatters from the left-moving Fermi point $k_{\text{F,left-moving}}$ ($k_{\text{FA}}+$, $k_{\text{FB}}-$) to the right-moving Fermi point $k_{\text{F,right-moving}}$ ($k_{\text{FA}}-$, $k_{\text{FB}}+$), while the other electron scatters from $k_{\text{F,right-moving}}$ to $k_{\text{F,left-moving}}$. The momentum transfer is ($k_{\text{F,left-moving}} - k_{\text{F,right-moving}}$), and electrons change propagating direction after each scattering process. This is denoted by backward scattering. If the spin of the two scattered electrons are parallel, then the coupling constants are labeled with subscript //, while the spin antiparallel cases are labeled by the subscript $\perp$. In the g_2-type process, the momentum transfer from one electron to another is zero, and the propagating direction remains unchanged. This process is usually denoted as forward scattering. However, in the g_2 scattering process one electron must come from states near $k_{\text{F,right-moving}}$ while the other must come from $k_{\text{F,left-moving}}$. Each combination of left-moving and right-moving pair constitutes an interaction channel, and in each channel there are $g_{1//}$, $g_{1\perp}$, and g_2 type couplings. The six channels are shown in Fig. 1.6(a–f) with the g_1-type scattering processes. With these interaction coupling constants, the Hamiltonian with electron–electron interaction in a (5,0) CNT can be expressed as

$$\begin{aligned} H = & \sum_{\alpha=\uparrow\downarrow} \sum_{m=A,A',B} \sum_{k} (\varepsilon_{k_f m} a^{+}_{km\alpha} a_{km\alpha} + \varepsilon_{-k_f m} b^{+}_{km\alpha} b_{km\alpha}) \\ & + \sum_{\alpha,\beta} \sum_{n=1-6} \sum_{k,p,q} (g_n^{1//} a^{+}_{kn\alpha} b^{+}_{pn\beta} a_{p+2k_F+q,n,\beta} b_{k-2k_F-q,n,\alpha} \delta_{\alpha,\beta} \\ & + g_n^{1\perp} a^{+}_{kn\alpha} b^{+}_{pn\beta} a_{p+2k_F+q,n,\beta} b_{k-2k_F-q,n,\alpha} \delta_{\alpha,-\beta} + g_n^{2} a^{+}_{k\alpha} b^{+}_{p,\beta} b_{p+q,\beta} a_{k-q,\alpha} \delta_{\alpha,-\beta}), \end{aligned} \tag{1.2}$$

in which $n = 1$–6 denotes the six different interacting channels shown in Fig. 1.6(a–f), p, q k are the momentum indices. If we consider the (5,0) CNT to be embedded in array structure that comprises a central nanotube with six nearest neighbor nanotubes, arranged hexagonally and separated from each other by 1 nm, then there will be an additional 12 inter-tube coupling channels with 36 coupling constants. These additional scattering processes can be denoted by just replacing the 2 of 4 operators with the corresponding operators in the nearest-neighbor tube.

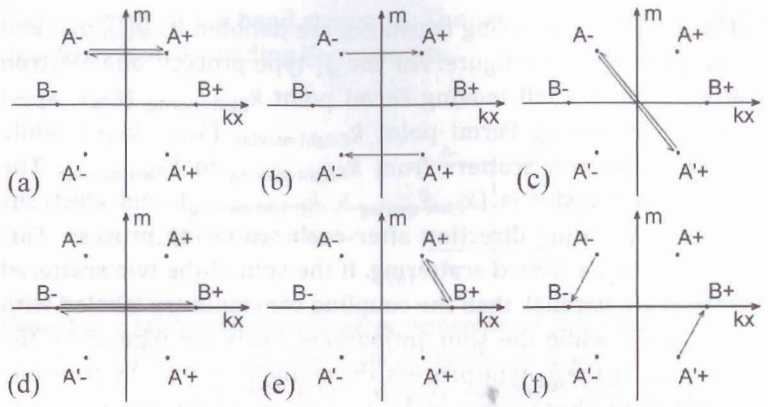

Figure 1.6 (a–f) The six interaction channels in an individual (5,0) CNT. For each channel, the two electrons are from two bands with opposite Fermi velocities. There are six different combinations each, selecting two Fermi points with opposite Fermi velocities among the six Fermi points, namely A±, A′±, and B±, so that there are six interaction channels in total. The scattering processes shown are the g_1 type. Adapted from Ref. [39].

1.3.2 RG Treatment of a Single (5,0) Nanotube

The difficulty in handling 1D interacting electrons is that the perturbation expansion of the interaction vertex yields a logarithmically divergent Feynman integral in the long wavelength limit. The central idea of the RG method is to (differentially) change the energy cutoff in the Feynman diagram integral to a smaller value and to collect the resulting effect as a change in the coupling constants. Since, under the new cutoff, the $\log(\omega/E_C)$ function is less divergent (as ω approaches zero so the logarithm is negative), by performing this process iteratively one can get a set of evolution equations for the coupling constants and response functions, denoted scaling equations. There are several approaches to derive the RG scaling equations in the 1D Fermion systems. Here, we employ the multiplicative RG method [32,33]. With this approach, we can easily derive the RG scaling equations up to any order. This is important because the first-order RG is not enough to treat systems with the attractive interaction. It is only by going to the second-order RG will the meaningful results be obtained.

The multiplicative RG is performed as follows for each coupling constant:

$$g_n^{i\prime}\tilde{\Gamma}_n^i\left(\frac{k}{k_C'},\frac{\omega}{E_C'},g_n^{i\prime}\right)d_m^2\left(\frac{k}{k_C'},\frac{\omega}{E_C'},g_n^{i\prime}\right) = g_n^i\tilde{\Gamma}_n^i\left(\frac{k}{k_C},\frac{\omega}{E_C},g_n^i\right)d_m^2\left(\frac{k}{k_C},\frac{\omega}{E_C},g_n^i\right), \tag{1.3a}$$

$$\Gamma_n^{\alpha\beta\gamma\delta}(k,\omega) = g_n^{1//}\tilde{\Gamma}_n^{1//}\left(\frac{k}{k_C},\frac{\omega}{E_C}\right)\delta_{\alpha\gamma}\delta_{\beta\delta}\delta_{\alpha\beta} + g_n^{1\perp}\tilde{\Gamma}_n^{1\perp}\left(\frac{k}{k_C},\frac{\omega}{E_C}\right)\delta_{\alpha\gamma}\delta_{\beta\delta}\delta_{\alpha,-\beta} - g_n^2\tilde{\Gamma}_n^2\left(\frac{k}{k_C},\frac{\omega}{E_C}\right)\delta_{\alpha\delta}\delta_{\beta\gamma}, \tag{1.3b}$$

$$G_m(k,\omega) = d_m\left(\frac{k}{k_C},\frac{\omega}{E_C}\right)G_m^{(0)}(k,\omega), \tag{1.3c}$$

where Eq. (1.3a) describes the relationship between the coupling constants with the original and the scaled energy cutoff. The dimensionless vertex for each interaction channel $\tilde{\Gamma}_n^i$ ($n=1$–6, $i=1//$, $1\perp$, 2) in Eq. (1.3a) are defined in Eq. (1.3b), and the dimensionless Green function d_m (m = A, A′, B) is defined in Eq. (1.3c). With this set of equations, the coupling constants with new g_i's can be related to their corresponding original values. Following the diagram expansion calculation shown in Figs. 1.7 and 1.8, together with the attendant multiplicative relation of Eq. (1.3), we obtain the scaling equations for the coupling constants as temperature decreases to zero. If we consider only the diagrams shown in Fig. 1.7(a,b), the results obtained pertain to the first-order RG. If we consider the superconductivity problem, i.e., in the presence of phonon-mediated electron–electron attractive interaction, then the first-order RG suffers from the divergence in the coupling constants and response functions at finite temperatures. This is unphysical since that would imply a sharp phase transition can occur (since a second-order phase transition is always characterized by the divergence in the response functions of the system) at finite temperatures for 1D systems, in violation of the Hohenberg–Mermin–Wagner Theorem. Hence we must go beyond the first-order RG and

take into account the diagrams shown in Fig. 1.7(c, d). These diagrams give rise to second-order correction to the RG scaling equations. At this second-order level the unphysical results are eliminated and divergence can only happen at zero temperature. The detailed scaling equations can be found in [39].

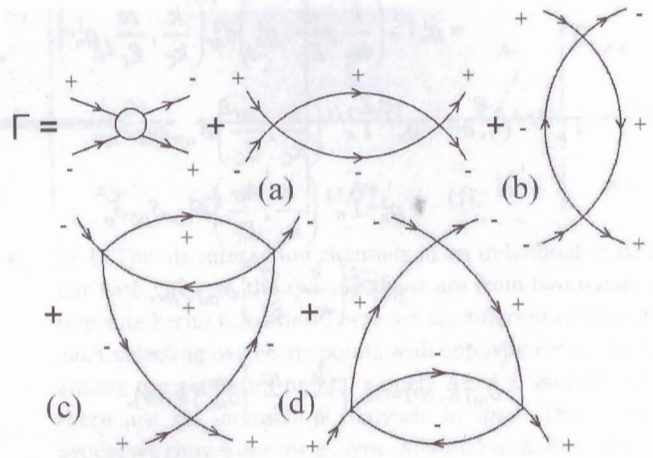

Figure 1.7 The expansion diagrams of the interaction vertex that are log divergent. The signs + and − mean that the electron/hole are right-moving and left-moving, respectively. Adapted from Ref. [32].

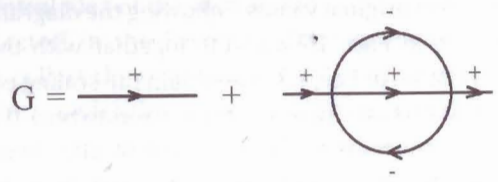

Figure 1.8 The self-energy correction to the Green function. Adapted from Ref. [32].

We are interested in determining the possible ground state(s) of the system. This objective is accomplished by calculating the response functions of the system. The response function is defined as the amplitude of the system response with respect to an external perturbation. The asymptotic behavior of coupling constants can be used to generate the response functions at temperatures

approaching zero. In 3D systems, phase transition is usually identified with the singularity found in response functions. However, in 1D, since no phase transitions can occur at finite temperatures, owing to the Hohenberg–Mermin–Wagner Theorem, hence response functions should be divergent only at zero temperature. This condition is only satisfied if we use the second-order RG correction, with the resulting power law–divergent response function(s) $R(\omega/E_C) \sim (\omega/E_C)^{\alpha}$, $\alpha < 0$.

In each interaction channel depicted in Fig. 1.6(a–f), there are four types of response functions that need to be taken into account, as they contain logarithmically singular terms up to any order of perturbative expansion. The four divergent response functions are the charge density wave–response function (CDW) $\overline{N}(\omega)$, i.e., the Peierls distortion response function (the response functions denoted with the over-bar are actually the auxiliary function of the corresponding response functions, see [32]), the spin-density-wave response function (SDW) $\overline{\chi}(\omega)$, the singlet superconductivity response function (SS) $\overline{\Delta_s}(\omega)$, and the triplet superconductivity response function (TS) $\overline{\Delta_t}(\omega)$. Since they are all divergent, the ground state is identified by the one whose response function is the *most singular* when temperature decreases to zero. The scaling equations for the four types of response function are:

$$\frac{d\ln\overline{N_n}(x)}{dx} = \frac{1}{x}\left\{\frac{1}{\pi\upsilon_F}\left[g_n^{1//} + g_n^{1\perp} - g_n^2\right] + \cdots\right\} \tag{1.4a}$$

$$\frac{d\ln\overline{\chi_n}(x)}{dx} = \frac{1}{x}\left\{\frac{1}{\pi\upsilon_F}\left[-g_n^2\right] + \cdots\right\} \tag{1.4b}$$

$$\frac{d\ln\overline{\Delta_{S,n}}(x)}{dx} = \frac{1}{x}\left\{\frac{1}{\pi\upsilon_F}\left[g_n^{1\perp} + g_n^2\right] + \cdots\right\} \tag{1.4c}$$

$$\frac{d\ln\overline{\Delta_{T,n}}(x)}{dx} = \frac{1}{x}\left\{\frac{1}{\pi\upsilon_F}\left[-g_n^{1//} + g_n^2\right] + \cdots\right\} \tag{1.4d}$$

With given initial values of the coupling constants, we can obtain the most singular response function that characterizes the ground states (as T approaches zero) by solving Eq. (1.4). Here, $x = \log(\omega/E_C)$.

1.3.3 Scaling Results for a Single (5,0) CNT

Following the method described above, we have performed second-order RG analysis on a single (5,0) CNT, as well as on a thin array of (5,0) CNTs. The results of the RG analysis are the fixed points and their corresponding phase diagram. We use physically relevant initial values of the coupling constants for the RG scaling equations and track the system behavior when the temperature decreases to zero. Since the final results clearly depend on the initial values of the coupling constants, attention must be paid to this aspect of the problem. We have followed the analysis of Perfetto et al. [40] to estimate the initial values of the coupling constants. There are two physical mechanisms in the electron–electron interaction. The first one is the Coulomb interaction, which is repulsive; hence, the interaction constant is positive in value. The second one is phonon-mediated interaction, which is attractive and hence negative in value. The initial values of the dimensionless coupling constants represent the sum of these two mechanisms. For an individual (5,0) CNT, the initial values are (with $g^{1\perp} = g^{1//}$):

$$\frac{g_1^{1\perp}}{2\pi\upsilon_A}, \frac{g_2^{1\perp}}{2\pi\upsilon_A} = -0.095 + 0.573/\kappa,$$

$$\frac{g_1^2}{2\pi\upsilon_A}, \frac{g_2^2}{2\pi\upsilon_A}, \frac{g_4^2}{2\pi\upsilon_A}, \frac{g_5^2}{2\pi\upsilon_A} = 15.9/\kappa,$$

$$\frac{g_4^{1\perp}}{2\pi\upsilon_A} = -0.175 + 0.175/\kappa,$$

$$\frac{g_5^{1\perp}}{2\pi\upsilon_A}, \frac{g_6^{1\perp}}{2\pi\upsilon_A} = -0.0796 + 0.0796/\kappa,$$

$$\frac{g_6^2}{2\pi\upsilon_A} = -0.0796 + 0.0478/\kappa,$$

$$\frac{g_3^2}{2\pi\upsilon_A}, \frac{g_3^{1\perp}}{2\pi\upsilon_A} = -0.0796 + 0.0079/\kappa.$$

It should be noted that these values are dependent on the dielectric constant κ of medium. In vacuum with $\kappa = 1$, the values of the fixed points are:

$$\frac{g_1^2}{2\pi\upsilon_A} \to 16.05,$$

$$\frac{g_2^2}{2\pi\upsilon_A}, \frac{g_4^2}{2\pi\upsilon_A} \to 15.55,$$

$$\frac{g_3^2}{2\pi\upsilon_A} \to -0.5,$$

$$\frac{g_5^{1\perp}}{2\pi\upsilon_A} \to -2/3,$$

$$\frac{g_5^2}{2\pi\upsilon_A} \to 15.71,$$

$$\frac{g_6^{1\perp}}{2\pi\upsilon_A} \to 0.76.$$

All other coupling constants scale to zero. Since the response functions are power law divergent as $R(x) \sim x^{\alpha}$, the value of exponent α determines the relative relationship of the different response functions. From Eq. (1.4), the power law exponent α is $\sim[g_{1//} + g_{1\perp} - g_2]/\pi\upsilon_F$ (as T approaches 0) for the CDW (Peierls distortion) response function, $\sim[-g_2]/\pi\upsilon_F$] for the SDW response function, $\sim[g_{1\perp} + g_2]/\pi\upsilon_F$ for SS response function, and $\sim[-g_{1//} + g_2]/\pi\upsilon_F$ for the TS response function. In each interacting channel, there are four corresponding response functions, and substituting the fixed point values of the coupling constants into Eq. (1.4), we find in this particular case the CDW and SDW response functions are the most divergent. Hence, they represent the ground state.

If the individual (5,0) CNT is embedded in a dielectric medium with $\kappa > 1.15$, the fixed point values of the coupling constants are κ-dependent:

$$\frac{g_1^{1\perp}}{2\pi\upsilon_A}, \frac{g_5^{1\perp}}{2\pi\upsilon_A} \to 0,$$

$$\frac{g_1^2}{2\pi\upsilon_A}, \frac{g_5^2}{2\pi\upsilon_A} \to 0.268 + 15.03/(\kappa - 0.064),$$

$$\frac{g_2^2}{2\pi\upsilon_A}, \frac{g_4^2}{2\pi\upsilon_A} \to \frac{g_1^2}{2\pi\upsilon_A} - 1,$$

while all other coupling constants scales to the fixed point value of -1. In this case, if $\kappa > 22$, then the SS response function in channels 2 and 6 overcomes the CDW in channels 3 and 4 to become the most divergent one. If $\kappa < 22$, then CDW would be the most divergent.

This result is consistent with the statement that a single (5,0) CNT will undergo a Peierls transition under usual conditions [12–17].

1.3.4 Scaling Results for a Thin Array of (5,0)

In our experiments, the (5,0) CNTs are embedded in a hexagonal close-packed array of other (5,0) CNTs, with the AFI zeolite framework serving as the dielectric medium. In this case, the situation is quite different. As mentioned above, there are additional inter-tube electron–electron interactions that can affect both the scaling equations and the initial values of the coupling constants. We must take into account new possible intermediate states in the derivation of the scaling equations not only for the 6 intra-tube channels, but also for the additional 12 inter-tube channels for a thin array that comprises one central (5,0) CNT surrounded by six identical (5,0) CNTs in the hexagonal configuration with a wall-to-wall separation of 1 nm. For the initial values of the coupling constants, the existence of other metallic CNTs that are separated from the nearest neighbors by only 1 nm will greatly screen and reduce the Coulomb repulsive interaction strength, and thereby qualitatively influence the fixed points [40]. Without giving the details that can be found in [39], in the thin array configuration, the screened initial values of the coupling constants are as follows:

$$\frac{g_1^2}{2\pi v_A}=\frac{g_2^2}{2\pi v_A}=\frac{g_4^2}{2\pi v_A}=\frac{g_5^2}{2\pi v_A}\sim 0.1,$$

$$\frac{\overline{g_1^2}}{2\pi v_A}=\frac{\overline{g_2^2}}{2\pi v_A}=0.00032\kappa,$$

$$\frac{\overline{g_1^{1\perp}}}{2\pi v_A}=\frac{\overline{g_2^{1\perp}}}{2\pi v_A}=0.045/\kappa,$$

in which $\overline{g_n^j}$ denotes the inter-tube couplings. In the array configuration, the initial values of the forward scatterings are about two orders of magnitude smaller than that in the individual CNT case. So the fixed points are significantly modified from those of the individual CNTs. If the dielectric constant $\kappa < 1.38$, then all response functions still remain small. If we take the dielectric constant of AFI framework to be >1.38, e.g., $\kappa \sim 6$ for aluminophosphate (the composition of the AFI zeolite), then the fixed points are:

$$\frac{g_1^2}{2\pi v_A},\frac{g_5^2}{2\pi v_A}\to 0.287,$$

$$\frac{g_2^2}{2\pi v_A},\frac{g_4^2}{2\pi v_A}\to\frac{g_1^2}{2\pi v_A}-1=-0.713.$$

All other coupling constants are noted to scale to −1. Therefore, in the array configuration, the most divergent response function is the SS response function, with $\alpha \sim -0.573, -4, -3.427, -3.427, 0.573,$ and -4 in the six intra-tube channels as shown in Fig. 1.6(a–f), respectively. The next divergent one is the CDW response function, with $\alpha \sim -0.573, -2, -2.573, -2.573, -0.573,$ and -2, listed in the same order. A sketch of the CDW and SS response functions in channels 1 and 4 (these two channels are associated with electrons in only the A band and the B band, respectively) are shown in Fig. 1.9, in which the SS response in the B band (channel 4) is more divergent than others as ω approaches zero. It follows that under the condition of our experiments, the (5,0) nanotube array should be superconducting at zero temperature.

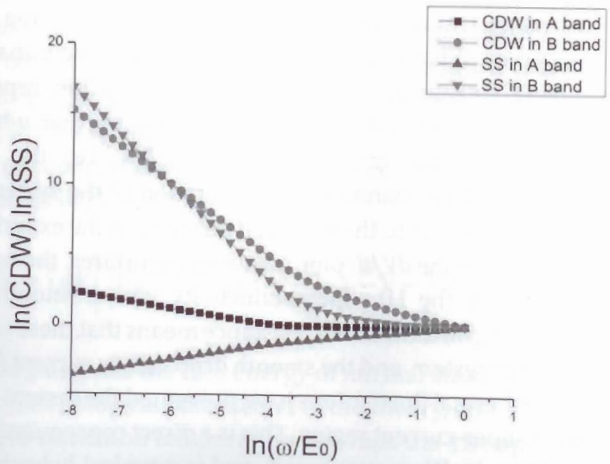

Figure 1.9 The scaling flow of CDW and SS in the A band and B band. As ω approaches zero, the SS response in the B band is seen to be the most divergent. Hence, superconductivity is the ground state for the thin array configuration.

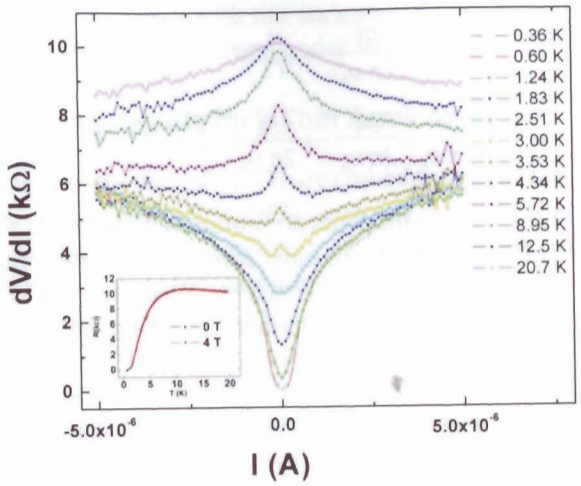

Figure 1.10 The experimental data of differential resistance under different current/voltage and temperature. We can see that at low temperatures, typical 1D superconducting behavior was observed, but with increasing temperature, a peak in dV/dI arises at zero bias. This is attributed to the excitation of the CDW state that can lead to a quasi-gap around the Fermi level. Adapted from Ref. [39].

An interesting feature shown in Fig. 1.9 is the crossing of the two scaling curves. What this means is that owing to the initial value of the coupling constants, the CDW response function represents the dominant one at higher temperatures, implying that while the superconductivity is the ground state, the CDW, i.e., the Peierls distortion state, may be manifest as an excitation of the system. This feature can be the answer to the observed behavior in the experiments, shown in Fig. 1.10. In the dV/dI plot, at low temperatures, the behavior shown is typical for the 1D superconductivity, with a smooth dip at current $I=0$. The dip in differential resistance means that there is super-current inside the system, and the smooth drop versus current/voltage means that the thermal fluctuations have prevented the system to form a well-defined super-current region. This is a direct consequence of the Hohenberg–Mermin–Wagner theorem and is a typical behavior for a 1D superconductor. In the inset of Fig. 1.10 is shown the temperature dependence of the measured resistance. Again, a smooth decrease of the resistance, which is independent of the magnetic field, is a manifestation of the 1D superconductivity. Therefore, we attribute

this result to a very thin CNT array whose cross-sectional dimension is less than a coherence length. When the temperature increases, however, a peak is seen to arise. A peak in the differential resistance is indicative of the appearance of a quasi-gap in DOS. We attribute the peak at higher temperatures to the appearance of CDW excitations.

1.4 Appearance of Thermal Fluctuation–Induced Resistance in 1D Superconductors

The RG analysis in the previous section shows the Cooper-pair condensation to be the most favorable state in the CNT@AFI system when temperature decreases to zero. However, to better understand the experimental results, it is necessary to appeal to phenomenological theory, which will be the GL theory of superconductivity [42] plus its 1D version, the Langer–Ambegaokar–McCumber–Halperin theory [21,43–45]. In this section, we give a brief description on the appearance of resistance in 1D superconductors, such as that shown in the inset to Fig. 1.10. In Section 1.5, we shall detail how a weak transverse Josephson coupling between the (5,0) CNTs can effect a transition to a 3D superconducting state (at a temperature below that at which the 1D superconducting condensate first appears), together with a sharp resistive transition and the attendant interesting behaviors.

The basic concept of the GL theory is to define a coarse-grained complex order parameter, or "wave function" of the system, $\psi(\vec{r}) = |\psi(\vec{r})| \exp[i\varphi(\vec{r})]$ with $|\psi(\vec{r})|^2 = n_S(\vec{r})$ being the local density of superconducting electrons. The free energy of the system is written as [42]:

$$F = F_N + \int dV \left(\alpha|\psi|^2 + \frac{\beta}{2}|\psi|^4 + \frac{1}{2m^*}\left|\left(\frac{\hbar}{i}\nabla - \frac{q}{c}\vec{A}\right)\psi\right|^2 + \frac{B^2}{8\pi}\right), \quad (1.5)$$

in which F_N denotes the free energy of normal state, $\alpha = a(T - T_C^0)$, β are phenomenological parameters of the theory, and T_C^0 denotes the mean-field transition temperature at which the 1D superconducting condensate appears. The mass and charge of a Cooper-pair are $m^* = 2m$ and $q = 2e$, respectively, and $\vec{A}$ and $\vec{B} = \nabla \times \vec{A}$ are the vector potential and magnetic field, respectively. Variationally minimizing the free energy with respect to ψ and $\vec{A}$ leads to the GL differential equations:

$$\alpha\psi+\beta|\psi|^2\psi+\frac{1}{2m^*}\left(\frac{\hbar}{i}\nabla-\frac{q}{c}\vec{A}\right)^2\psi=0, \tag{1.6}$$

$$\vec{j}=\frac{1}{\mu_0}\nabla\times\vec{B}=\frac{q\hbar}{2m^*i}(\psi^*\nabla\psi-\psi\nabla\psi^*)-\frac{q^2}{m^*c}|\psi|^2\vec{A}. \tag{1.7}$$

If we substitute $\psi(\vec{r})=|\psi(\vec{r})|\exp[i\varphi(\vec{r})]$ into Eq. (1.7), we get

$$\vec{j}=-\frac{e|\psi|^2\hbar}{m}\left(\frac{2\pi}{(hc/2e)}\vec{A}-\nabla\varphi\right). \tag{1.8}$$

Equation (1.8) shows that besides the vector potential, the current density inside a superconductor is proportional to the spatial derivative of the phase $\varphi(r)$. This is important for understanding the origin of resistance in 1D superconductors, shown below.

In a superconductor, the coherence length ξ is defined as the length scale that characterizes the spatial variation of the order parameter ψ, i.e., $\xi=\sqrt{\frac{\hbar^2}{2m|\alpha|}}=\xi_0\left|\frac{T_C^0}{T_C^0-T}\right|^{1/2}$, where ξ_0 is the coherence length at zero temperature.

In a 1D superconductor, the GL order parameter is only a function of the x-coordinate. This is because the cross-sectional dimension of the sample is by definition smaller than a coherence length; therefore, the order parameter can be regarded as a constant along the two other directions. Then, the free energy of system can be simplified to the following form at zero magnetic field [21,43–46]:

$$F[\psi(x)]=\sigma\int dx\left(\frac{\hbar^2}{2m^*}|\nabla\psi(x)|^2+\alpha|\psi(x)|^2+\frac{\beta}{2}|\psi(x)|^4\right), \tag{1.9}$$

where σ denotes the cross-sectional area of the 1D superconductor. The corresponding time-dependent GL equation, which describes the time evolution of ψ, is given by

$$\gamma\frac{\partial}{\partial t}\psi=-\frac{1}{\sigma}\frac{\delta F[\psi]}{\delta\psi}+\zeta=\frac{\hbar^2}{m^*}\nabla^2\psi-2\alpha\psi-2\beta|\psi|^2\psi+\zeta. \tag{1.10}$$

Here, γ is a viscosity coefficient, and the ζ denotes the Langevin white noise, associated with the fluctuation effect of the heat bath.

The steady-state solution of this equation, without the noise, can be obtained by setting the time derivative of ψ equal to zero. If we rescale ψ by $\sqrt{-\alpha/\beta}$, x by coherence length ξ, and time by $-\gamma/\alpha$, and impose periodic condition, i.e., setting $\psi(-L/2)=\psi(L/2)$, L being the length of the 1D superconductor, Eq. (1.10) simplifies to

$$0=\frac{\partial}{\partial\bar{t}}\bar{\psi}=\nabla^2\bar{\psi}+\bar{\psi}-\beta|\bar{\psi}|^2\bar{\psi}, \tag{1.11}$$

which has the solution

$$\bar{\psi}_n(x)=\sqrt{1-k_n^2}e^{ik_nx},\ k_n=2\pi n/L. \tag{1.12}$$

Here, n is an integer called the winding number, and k_n serves as a wave vector. It should be noted that Eq. (1.12) is really not a plane-wave solution, since the amplitude of e^{ik_nx}, $\sqrt{1-k_n^2}$, depends on k_n owing to the nonlinear character of Eq. (1.11). By using the quantum mechanical formula for the current density, the steady-state solution given by Eq. (1.12) carries a current density $J_n=(1-k_n^2)k_n$, with $|k_n|<k_C=1/\sqrt{3}$ being the upper bound of the permitted wave vectors. A schematic picture of the current-carrying state with $n=4$ is given in Fig. 1.11 [46].

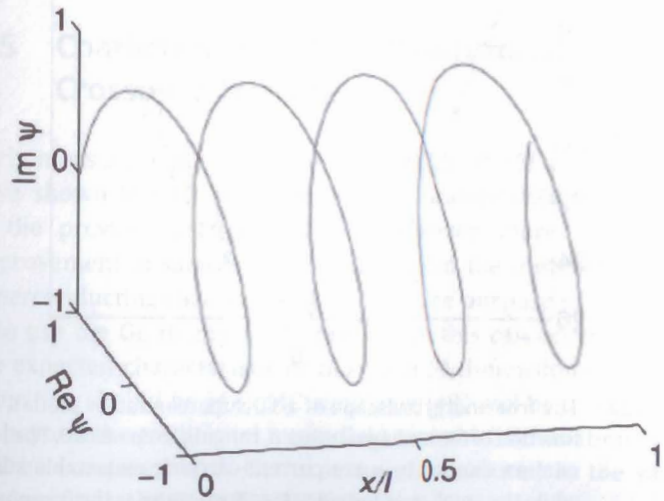

Figure 1.11 A schematic plot of the current-carrying state with a winding number $n=4$. Adapted from Ref. [46].

Each current-carrying steady state is characterized by a winding number n. Larger the n, larger the current and also higher the free energy. By using the string method, one can map out the free energy landscape from one steady-state solution to the next. In Fig. 1.12, we show the energy landscape for a 1D superconductor along the *path of minimum energy* in the functional space. It should be noted that between two nearest-neighbor current-carrying states, there exists a barrier preventing the system from slipping from one state to its neighboring state. In other words, each steady-state solution is located at a local minimum of the free energy, and when the state is in such a local minimum, the system displays no resistance, i.e., the system is superconducting. However, at finite temperatures, there will always be the chance of thermal excitation over the small barrier (whose magnitude is directly proportional to the cross-sectional area σ of the 1D superconductor) separating the different current-carrying states, e.g., from a higher winding number state to a lower winding number state. Hence, these current-carrying states are metastable at finite temperatures.

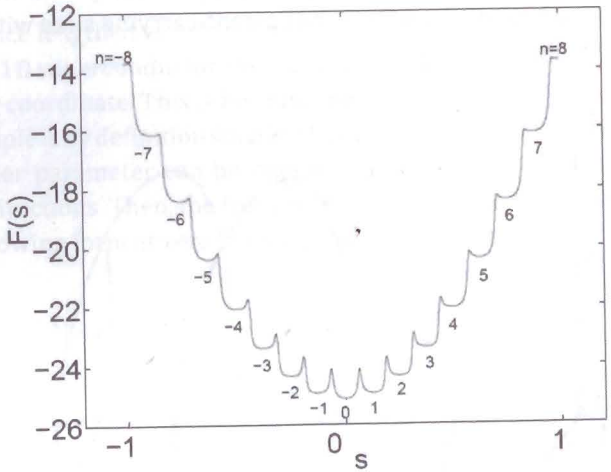

Figure 1.12 The free energy landscape of a 1D superconductor plotted as a function of the winding number n, ranging from −8 to 8. The local minima denoted by n are current-carrying metastable states, while the small peaks between two such states is the free energy barrier. Here, s is a path length parameter in the functional space of winding number configurations. Adapted from Ref. [46].

So far, we have described the metastable state $\overline{\psi}_n(x)$ inside a 1D superconductor, which carries a current density J_n, without any dissipation. However, in the presence of the Langevin white noise term ζ, thermal fluctuations would cause the system to overcome the free energy barrier separating two metastable states with different winding number n, thereby one current-carrying state can transit into another. In this process, both the free energy as well as the current would change. If the 1D superconductor is connected to a constant-current source, as in many experiments, then the current source will restore the original current state by pushing the state up in energy. In doing so, work will be done by an external source; hence, dissipation has occurred, i.e., resistance appears. Since the resistance is directly proportional to the rate of transitions between the different current-carrying states, it follows that higher the temperature, higher the resistance. Also, since the free energy barrier is lower for the higher current-carrying states, the transition rate between different current states will be higher with increasing (external) bias current. Therefore, the resistance will increase with either increasing temperature or increasing bias current. This is a physical explanation for the observed resistance in 1D superconducting systems.

1.5 Characteristics of the Dimensional Crossover Transition

Early measurements on the 4-Angstrom CNT@AFI zeolite crystals have shown the 1D superconducting characteristics as described in the previous section [1,20,21]. However, more recently the improvement in sample quality has enabled the observation of 3D superconducting characteristics [19,21]. The purpose of this section is to use the GL theory [42] to show how this can occur and what the expected characteristic of the 1D to 3D dimensional crossover transition should be [47]. MC simulation [48] will be used, so as to go beyond the traditional mean field treatment. Simulation results will be compared with the experiments, measured in the sample configuration shown in Fig. 1.13.

Since the 4-Angstrom CNTs are aligned in the array of 1D pores of the AFI, the wall-wall separation is only 9.6 Å, which allows

a Josephson coupling in the a–b plane. Because the CNTs are segmented and randomly distributed in the pores of AFI, the system is inhomogeneous. The Josephson coupling is obviously dependent on the overlap between the neighboring nanotubes along the c-axis direction. Stronger couplings can result from significant overlaps, whereas very weak couplings would be the case with small overlaps. In our simplified model, the strongly coupled nanotubes are regarded as constituting a quasi-1D nanowire, and these nanowires form a 2D triangular lattice in the x–y (a–b) plane with their c-axes aligned along z-coordinate as shown in Fig. 1.14 [47]. The interaction between the nanowires is much weaker as compared with that along the c-axis of the nanowires. This model can capture the essential characteristics of our samples.

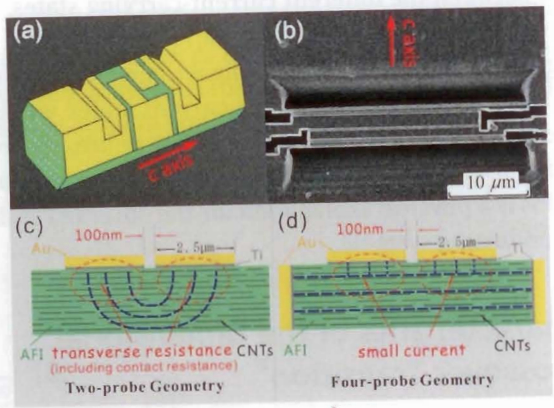

Figure 1.13 (a) A cartoon picture of the sample configuration in the experiment. Green denotes the AFI crystal, in which open circles denote CNTs. Yellow is gold, which is part of the electrode. Focused ion beam was used to delineate the top electrodes by etching away the gold to expose the AFI crystal surface. (b) SEM image of the sample. Red arrow indicates the position of the c-axis. The thin line in the middle divides the two surface electrodes. The two troughs on the top and bottom correspond to the current electrodes in the four-probe measurement geometry. (c) and (d) are schematic drawings of the two-probe and four-probe measuring geometries on the side view. Blue dashed lines denote the current. We can see the two-probe measurement results include the transverse resistance, but the four-probe measurement is mainly on the c-axis resistance. Adapted from Ref. [19].

Figure 1.14 A cartoon picture of the model. The parallel nanowires form a 2D triangular lattice in x-y (a–b) plane. The nearest-neighbor nanowires interact with each other by weak Josephson coupling, denoted by the double-headed arrows. Adapted from Ref. [47].

The above model has been studied extensively in the mean-field approximation, and a 3D long-range ordered state can be found at low temperatures [49–57]. However, the behavior near the critical temperature attracts little attention [51]. In particular, the specific heat and the phase correlation in the a–b plane, which are crucial to the interpretation of the experimental data on 4-Angstrom CNTs, have not been studied. Hence, in the following, we use MC simulation on the GL theory to analyze the behavior of the specific heat and the electronic transport in this model and to compare the results with the experimental observations [19,20].

In dimensionless form, the GL free energy functional for the weakly coupled quasi-1D nanowires can be expressed as

$$\begin{aligned}\bar{F}_{\mathrm{GL}} = \frac{F_{\mathrm{GL}}}{\varepsilon_0 k_{\mathrm{B}} T_{\mathrm{C}}^0} = \sum_{i,j} \int d^3\bar{r} \Bigg[& 2(t-1)\left|\bar{\psi}_{i,j}\right|^2 + \left|\bar{\psi}_{i,j}\right|^4 \\ & + \sum_{\mu=x,y,z} 2\left|\left(-i\bar{\partial}_\mu - 2\pi \bar{A}_\mu\right)\bar{\psi}_{i,j}\right|^2 \Bigg] \\ & + \sum_{\langle ij,i'j'\rangle} \int d\bar{z}\, \bar{J}_{xy} \left|\bar{\psi}_{i,j}(z)\right| \left|\bar{\psi}_{i',j'}(z)\right| \\ & \left[1 - \cos\left(\phi_{i,j} - \phi_{i',j'}\right)\right].\end{aligned} \tag{1.13}$$

The first term expresses the GL free energy of the individual nanowires, whereas the second term is the energy of Josephson coupling between the nearest-neighbor nanowires. The indices i, j denote the coordinate of a nanowire in the x–y plane, $\bar{\psi}_{i,j} = \psi_{i,j} / |\psi_0|$, $\psi_{i,j}(\vec{r}) = |\psi_{i,j}(\vec{r})| \exp(i\phi_{i,j})$ is the GL order parameter, $|\psi_0| = \sqrt{aT_{\mathrm{C}}^0/\beta}$ is the zero-temperature mean-field value of $|\psi_{i,j}|$, where a and β are

two phenomenological parameters, T_C^0 denotes the nominal mean-field phase transition temperature at which the 1D superconducting condensate first appears, $t = T/T_C^0$, $\varepsilon_0 = a^2 {T_C^0}^2 \xi_{x0}\xi_{y0}\xi_{z0}/2\beta k_B T_C^0$ is the zero-temperature condensation energy within the volume $\xi_{x0}\xi_{y0}\xi_{z0}$, in units of $k_B T_C^0$; $\xi_{\mu 0} = \hbar/\sqrt{2m_\mu a T_C^0}$ is the zero-temperature coherence length along the μ(=x, y, z) direction, m_μ is the effective mass for one Cooper pair, $\bar{A}_\mu = A_\mu \xi_\mu/\Phi_0$, $\vec{A}$ is the vector potential, and $\Phi_0 = hc/2e$ is the flux quantum. Here, $\bar{J}_{xy} = 2J_{xy}/aT_C^0$ is the ratio between the Josephson interaction in the transverse direction and the GL free energy of the individual nanowires. In our model, this ratio is a very small number as shown below. Because the CNT in AFI is an extreme type II superconductor [20,58], the magnetic energy can be regarded as a constant in space and neglected. In the GL theory, the expectation value of a physical quantity Q can be evaluated as the ensemble average

$$\langle Q \rangle = \frac{\int D\psi Q \exp\{-F_{GL}[\psi]/k_B T\}}{\int D\psi \exp\{-F_{GL}[\psi]/k_B T\}}. \quad (1.14)$$

Here, $\int D\psi$ denotes the functional integration.

The specific heat is evaluated by using the Bardeen–Cooper–Schrieffer (BCS) specific heat expression [58]:

$$C = 2\beta^2 k_B \int g(\varepsilon)\exp(\beta E)\left[1+\exp(\beta E)\right]^{-2}\left(E^2 + \frac{1}{2}\beta\frac{d\Delta^2}{d\beta}\right)d\varepsilon. \quad (1.15)$$

Here, $\beta = 1/k_B T$, $E = \sqrt{\varepsilon^2 + \Delta^2}$, $g(\varepsilon) = N(0)\sqrt{1+\varepsilon/\varepsilon_F}$, ε_F is the Fermi energy, and $N(0)$ is the density of states (DOS) at the Fermi level. The gap function $\Delta(T, B)$ is evaluated by the GL theory, i.e., $[\Delta/\Delta(0)] = \sqrt{\left\langle |\psi|^2/|\psi_0|^2 \right\rangle}$ [20]. In this evaluation, the effect of the fluctuations is clearly manifested, and it is mainly the amplitude fluctuations that matter, in contrast to other effects shown below where phase fluctuations can be dominant. In the above, $\Delta(0)$ is the gap function at $B = 0$, $t = 0$, and $\Delta(0) = gk_B T_C^0$ with $g = 3$ fixed by the experimental data [20].

In comparison with the GL free energy of the individual nanowire, the Josephson interaction between nanowires is much smaller and can be neglected in the calculation of the specific heat. The specific heat peak arises from the contribution of the individual nanowires. The gap function $\Delta(T,B)$ can not be solved analytically from Eq. (1.13).

Thus, we discretize the nanowire and use MC simulation to obtain the gap function. Eq. (1.15) is then used to obtain the specific heat. The size of each nanowire is given by $L_x \times L_y \times L_z$. We simplify our model further and take $\xi_{x0} = \xi_{y0} = \xi_{z0} = \xi_0$. If the parameters are set to be $L_x = L_y = 3\xi_0$, $L_z \geq 64\xi_0$, $\xi_{\mu 0} = 13$ nm, $T_C^0 = 15$ K, and $\varepsilon_0 = 3$, the results, as well as the experimental data, are shown in Fig. 1.15. Good agreement is seen. Here, the rounded peak of the specific heat is a reflection of the large fluctuations in the quasi-1D nanowires [59], as compared with bulk superconductors. The peak is also noted to be shifted to lower temperature by the magnetic field. As the magnetic field can be associated with a length scale, the good agreement between theory and experiment tells us that each nanowire comprises an array of nanotubes with a cross-sectional dimension ~40 nm.

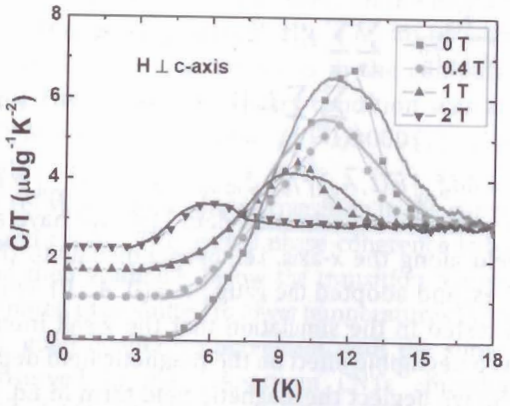

Figure 1.15 Theoretical and experimental results of specific heat in a magnetic field applied perpendicular to the *c*-axis of the nanowire. Solid lines denote the measured specific heat of superconducting carbon nanotubes embedded in AFI. The dots represent the simulated results in the simplified model with the parameters given in the text. The simulation results are normalized to the experimental data at one point of each curve. Adapted from Ref. [47].

Whereas the specific heat peak is mainly from the amplitude of the order parameter, the electronic transport is dominated by the phase of the order parameter, especially as the temperature is lowered from T_C^0 [44,45,60]. Even with a very weak Josephson interaction between nanowires, a dimensional crossover transition

can still occur. In order to study the effects of the weak Josephson coupling, we make the approximation, verified to be rather accurate, that in considering the phase effect between the nanowires the amplitude of the order parameter at any given temperature or magnetic field can be regarded as a constant. This approximation is especially true at temperatures much lower than T_C^0, since the amplitude fluctuations are inherently small.

Since the transverse phase fluctuations inside the individual nanowires are necessarily short wavelength in character, they are suppressed at low temperatures in comparison with the long-wavelength fluctuations along the *c*-axis. To a reasonably good approximation, the nanowires can be regarded as 1D without the transverse fluctuations in their cross sections. With all the above simplifications, Eq. (1.13) can be expressed in discretized form as

$$\bar{F}_{GL} = \frac{F_{GL}}{\varepsilon_0 k_B T_C^0} = \sum_{i,j}\sum_{k} J_z'[1-\cos(\phi_{i,j,k+1}-\phi_{i,j,k})] + \sum_{\langle ij,i'j'\rangle}\sum_{k} J_{xy}'[1-\cos(\phi_{i,j,k}-\phi_{i',j',k})]. \quad (1.16)$$

Here, $J_z' = 4d\xi_{z0}|\bar{\psi}(t,\bar{A}_y)|^2/\xi_{x0}\xi_{y0}$ and $J_{xy}' = d\bar{J}_{xy}|\bar{\psi}(t,\bar{A}_y)|^2/\xi_{z0}$. To compare with the experimental data [19], we have applied the magnetic field along the *x*-axis, i.e., perpendicular to the *c*-axis of the nanowires, and adopted the gauge $\bar{A} = (0, A_y, 0)$ with $A_y = -Bz$. It has been tested in the simulation that the weak inter-nanowire coupling has a negligible effect on the magnetic field dependence of the model. So we neglect the magnetic field term in Eq. (1.16). The effect of the magnetic field is manifest in the amplitude, $|\bar{\psi}(t,\bar{A}_y)|$, which is also a function of temperature. In the small region near the critical temperature of the dimensional crossover transition, J_{xy}' and J_z' can be regarded as constants, approximately, and our model becomes similar to the anisotropic 3D *x*–*y* model. Thus, we define the following quantities to describe the phase transition:

$$\eta = \frac{1}{N}\left\langle \left| \sum_{l=1}^{N} \exp(i\phi_l) \right| \right\rangle, \quad (1.17)$$

$$\Gamma(\vec{r}) = \langle\cos(\phi_{\vec{r}} - \phi_0)\rangle - \left(\langle\cos\phi_{\vec{r}}\rangle\langle\cos\phi_0\rangle + \langle\sin\phi_{\vec{r}}\rangle\langle\sin\phi_0\rangle\right), \quad (1.18)$$

$$\Delta\eta_z^2 = \frac{1}{N_z}\left\langle \left| \sum_{m=1}^{N_z} \exp(i\phi_m) - \frac{1}{N_z}\sum_{l=1}^{N_z} \exp(i\phi_l) \right|^2 \right\rangle. \quad (1.19)$$

Here, η is the phase-ordering parameter, which measures the overall phase coherence throughout the system. $\Gamma(\vec{r})$ is the correlation function. $\Delta\eta_z^2$ describes the phase fluctuations along the *c*-axis of the nanowires. It should be noted that our model differs from the 3D *x*–*y* model in that the *c*-axis behavior can also affect the system behavior.

MC simulation, with the Wolff algorithm [61], was employed to evaluate the above quantities in accordance with Eq. (1.14). The modulus, $|\bar{\psi}(t,\bar{A}_y)|$, can be obtained from $\langle|\bar{\psi}_{i,j}|\rangle$ in a similar way as in the computation of the gap function. The weak Josephson coupling has virtually no effect on the modulus. The size of the system is denoted by $N = N_x \times N_y \times N_z$. To be self-consistent, we use the same parameter values as in the computation of the specific heat. The periodic boundary condition was adopted. For $N_x = N_y = 60$, $N_z = 800$, the value of $\bar{J}_{xy} = 1/3000$ ($J_{xy}'/J_z' = 1/12{,}000$) was adopted.

In Fig. 1.16(a), a phase-ordering transition in the *a*–*b* plane can be seen at around $t = 0.5$. The overall phase coherence is built up, first abruptly and then gradually, below the transition temperature. The transition is noted to be shifted to lower temperatures by the magnetic field. It is in good qualitative agreement with the superconducting behavior observed in the 4-Angstrom CNTs embedded in AFI, shown in Fig. 1.16(c). It is also seen from Fig. 1.16(c) that below the transition (at around 5 K), the four-probe data (the magenta-colored curve) and the two-probe data (the light blue-colored curve) coincide. Since the difference between the two should be the transverse resistance in the *a*–*b* plane [see Figs. 1.13(c, d)], this implies the near-disappearance of resistance in the *a*–*b* plane. That is, the system has become 3D in character. Moreover, it is seen from Fig. 1.16(c) that the four-probe result (magenta curve) displays a kink followed by a sudden drop in the measured resistance at the transition, apparently reflecting the transverse coherence so that in effect the cross-sectional area (which would affect the barrier height separating the metastable current-carrying states, see the discussion in the previous section) of the 1D system has suddenly increased, thereby suppressing

the phase slip fluctuations. The decrease in the longitudinal phase fluctuation along the *c*-axis is revealed in Fig. 1.16(b). To obtain the simulation results shown in Fig. 1.16(b), the parameters $N_x = N_y = 12$, $N_z = 3200$ are set so as to capture more of the long-wavelength (phase) fluctuations along the *z*-direction (*c*-axis). The results with (shown in red) and without (shown in green) Josephson coupling are seen to suddenly deviate from each other at the transition temperature. The phase fluctuations along the *c*-axis show a sharp drop at the transition. The red curve in Fig. 1.16(b) corroborates well with the four-probe data shown in Fig. 1.16(c) (magenta line); whereas the green curve in Fig. 1.16(b) corroborates well with the four-probe data of the measured 1D behavior (as manifest in the smooth temperature dependence and magnetic field independence), shown in Fig. 1.16(d).

In order to uncover more details of the dimensional crossover transition in the *a*–*b* plane, we calculate the phase correlation function in *x*–*y* plane, with the focus on the behavior in the neighborhood of the transition temperature. To be consistent, the same parameters were used as in the computation of the phase-ordering parameter. The results are shown in Figs. 1.17(b,d). The correlation function decays exponentially as a function of distance in the *a*–*b* plane above the transition temperature. However, it decays in a power law manner below the transition temperature. This is the signature of a Berezinskii–Kosterlitz–Thouless (BKT) transition [62,63]. To verify this, in Fig. 1.17(c) we have evaluated the correlation length above the transition temperature and compared its temperature dependence with the predicted BKT behavior. Excellent agreement is seen. Since the temperature dependence of the resistance in a BKT transition is dictated by the behavior of the phase correlation length, it is expected that the measured 2-probe resistance, which is dominated by the transverse resistance in the *a*–*b* plane, should follow similar temperature dependence, and indeed it does, as shown in Fig. 1.17(a).

It should be mentioned that another manifestation of the BKT transition is the nonlinear *I*–*V* characteristics just above the T_C. That has indeed been observed experimentally [19] in the electrical differential resistance measurements and therefore offers additional support to the interpretation that the 1D to 3D dimensional crossover transition is mediated by a BKT transition in the *a*–*b* plane. However, the theoretical explanation of the nonlinear *I*–*V* behavior is beyond the present model.

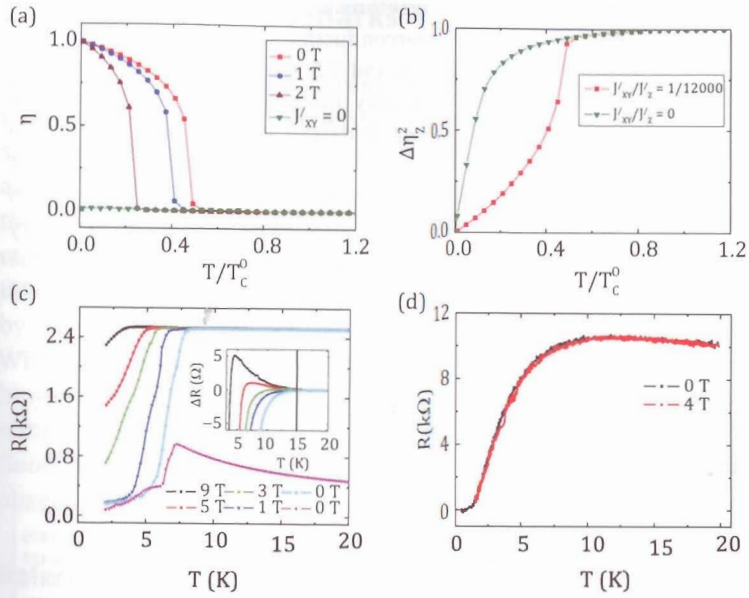

Figure 1.16 (a) Phase-ordering parameter as a function of the temperature and the magnetic field applied perpendicular to the *c*-axis of the nanowires. The green symbols denote the system without the weak transverse Josephson coupling between the nanowires, i.e., 1D system. The red, blue, and chocolate colors denote the cases with weak Josephson coupling, J'_{xy}/J'_z = 1/12,000, but under different applied magnetic field (shown in the legend). (b) The fluctuations along the *z*-direction, $\Delta\eta_z^2$, plotted as a function of temperature. Green denotes the case without Josephson coupling, i.e., a pure 1D system, whereas the red denotes the case with the weak Josephson coupling, $J'_{xy}/J'_z = 1/12{,}000$. It is seen that the fluctuations are suppressed below the transition temperature, owing to the dimensional crossover. (c) The measured resistance (in the sample configuration shown in Fig. 1.13) plotted as a function of temperature, for different magnetic field applied perpendicular to the *c*-axis of the nanotubes. The magenta curve is the data measured at zero field under the four-probes geometry, and the others are the two-probe data measured with the two surface electrodes (see Fig. 1.13c). Superconductivity is obviously suppressed by the magnetic field. The inset gives a magnified view of the upper section of the two-probe data,

(*Continued*)

which shows the magnetoresistance, and which reflects the appearance of the superconducting condensate, starts at 15 K. However, between 15 K and 7.5 K the system is basically 1D in character, hence display finite resistance that can arise from phase fluctuations as described in Section 1.4. (d) The resistance measured in the four-probe geometry for a different sample, which displays a pure 1D character as reflected in the smooth temperature dependence that corroborate very well with the green curve shown in (b), as well as in the magnetic field independence. Adapted from Ref. [19,20,47].

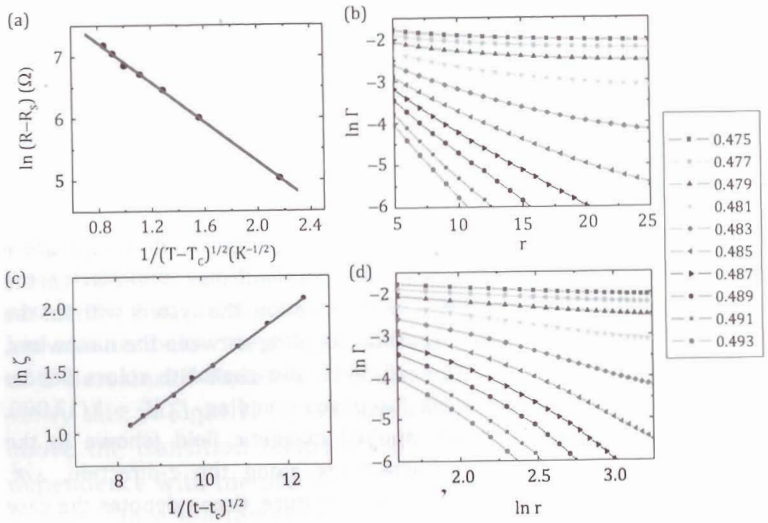

Figure 1.17 (a) The temperature dependence of resistance measured in the two-probe geometry, plotted in a manner as predicted by the BKT transition theory, i.e., $\ell n(R-R_S) \propto (T-T_C)^{-1/2}$ with $T_C = 6.17K$ and $R_S = 1.06\ k\Omega$. Here, the series resistance R_S was separately measured. (b) and (d) are the correlation functions in the x–y plane at different temperatures around the transition. They are the same data but plotted with different scales so as to emphasize the different behaviors. The correlation function decays as an exponential law above the transition but as a power law below the transition. This is the character of BKT transition. (c) The temperature dependence of the correlation length near the transition, plotted in the manner as predicted by the BKT transition, $\zeta = \zeta_0 \exp\left[c/\sqrt{t-t_C}\right]$, with t_C = 0.479, $\zeta_0 = 0.381$, $c = 0.245$. Adapted from Ref. [19,47].

1.6 Concluding Remarks

We have presented a coherent theoretical framework for the understanding of the experimental results on the observed superconductivity in 4-Angstrom CNTs. By using both RG technique as well as simulation on the phenomenological GL model, it is shown that in the array configuration, superconductivity can be the ground state of the system, winning over the Peierls distortion (CDW). However, the manifestation of superconductivity can be masked by phase slip fluctuations that are particular to the 1D systems. With weak transverse Josephson coupling between the nanotubes, however, there can be a dimensional crossover transition at a lower temperature, below which 3D superconducting behaviors appear. Good agreement is obtained between theory and experimental observations.

References

1. Z. K. Tang, L. Zhang, N. Wang, X. X. Zhang, G. H. Wen, G. D. Li, J. N. Wang, C. T. Chan and P. Sheng, *Science* **292**, 2462 (2001).
2. N. Wang, Z. K. Tang, G. D. Li and J. S. Chen, *Nature* **408**, 50 (2000).
3. Z. M. Li, Z. K. Tang, H. J. Liu, N. Wang, C. T. Chan, R. Saito, S. Okada, G. D. Li, J. S. Chen, N. Nagasawa and S. Tsuda, *Phys. Rev. Lett.* **87**, 127401 (2001).
4. Z. M. Li, H. J. Liu, J. T. Ye, C. T. Chan and Z. K. Tang, *Appl. Phys. A* **78**, 1121 (2004).
5. M. Hulman, H. Kuzmany, O. Dubay, G. Kresse, L. Li and Z. K. Tang, *J. Chem. Phys.* **119**, 3384 (2003).
6. Z. M. Li, Z. K. Tang, G. G. Siu, I. Bozovic, *Appl. Phys. Lett.* **84**, 4101 (2004).
7. H. J. Liu and C. T. Chan, *Phys. Rev. B* **66**, 115416 (2002).
8. M. Machon, S. Reich, C. Thomsen, D. S. Portal and P. Ordejon, *Phys. Rev. B* **66**, 155410 (2002).
9. I. Cabria, J. W. Mintmire and C. T. White, *Phys. Rev. B* **67**, 121406(R) (2003).
10. T. Miyake and S. Saito, *Phys. Rev. B* **68**, 155424 (2003).
11. L. X. Benedict, V. H. Crespi, S. G. Louie and M. L. Cohen, *Phys. Rev. B* **52**, 14935 (1995).
12. K. P. Bohnen, R. Heid, H. J. Liu and C. T. Chan, *Phys. Rev. Lett.* **93**, 245501 (2004).

13. K. P. Bohnen, R. Heid and C. T. Chan, *Phys. Rev. B* **77**, 235407 (2008).
14. D. Connetable, G. M. Rignanese, J. C. Charlier and X. Blase, *Phys. Rev. Lett.* **94**, 015503 (2005).
15. P. M. Singer, P. Wzietek, H. Alloul, F. Simon and H. Kuzmany, *Phys. Rev. Lett.* **95**, 236403 (2005).
16 B. Dora, M. Gulacsi, F. Simon and H. Kuzmany, *Phys. Rev. Lett.* **99**, 166402 (2007).
17. M. V. Fernandez-Serra and X. Blase, *Phys. Rev. B* **77**, 195115 (2008).
18. L. Chao, Z. Wang, W. Shi, Y. X. Wang, N. Wang, Z. K. Tang, P. Sheng and R. Lortz, *Phys. Rev. B* **83**, 184512 (2011).
19. Z. Wang, W. Shi, H. Xie, T. Zhang, N. Wang, Z. K Tang, X. X. Zhang, R. Lortz and P. Sheng, *Phys. Rev. B* **81**, 174530 (2010).
20. R. Lortz, Q. C. Zhang, W. Shi, C. Y. Qiu, Z. Wang, H. T. He, P. Sheng, T. Z. Qian, Z. K. Tang, N. Wang, X. X. Zhang, J. N. Wang and C. T. Chan, *Proceedings of the National Academy of Science of the United States of America* **106**, 7299 (2009).
21. Z. Wang, W. Shi, R. Lortz and P. Sheng, *Nanoscale* **4**, 21. (2012).
22. D. Mermin and H. Wagner, *Phys. Rev. Lett.* **17**, 1133 (1966).
23. P. C. Hohenberg, *Phys. Rev.* **158**, 383 (1967).
24. S. Tomonaga, *Prog. Theor. Phys.* **5**, 544 (1950).
25. J. M. Luttinger, *J. Math. Phys.* **4**, 1154 (1963).
26. D. C. Mattis and E. H. Lieb, *J. Math. Phys.* **6**, 304 (1965).
27. J. D. Delft and H. Schoeller, *Ann. Phys. (Leipzig)* **7**, 225 (1998).
28. A. O. Gogolin, A. A. Nersesyan and A. M. Tsvelik, *Bosonization and Strongly Correlated Systems* (Cambridge University Press Cambridge, UK, 1998).
29. J. Voit, *Rep. Prog. Phys.* **57**, 977 (1994).
30. M. Bockrath, D. H. Cobden, J. Lu, A. G. Rinzler, R. E. Smalley, L. Balents and P. L. McEuen, *Nature* **397**, 598 (1999).
31. C. L. Kane and M. P. A. Fisher, *Phys. Rev. B* **46**, 15233 (1992).
32. J. Solyom, *Adv. in Phys.* **28**, 201 (1979).
33. N. Menyhard and J. Solyom, *J. Low Temp. Phys.* **12**, 529 (1973).
34. R. Shankar, *Rev. Mod. Phys.* **66**, 129 (1994).
35. C. M. Varma and A. Zawadowski, *Phys. Rev. B* **32**, 7399 (1985).
36. K. Penc and J. Solyom, *Phys. Rev. B* **41**, 704 (1990).
37. J. Solyom, *J. Low Temp. Phys.* **12**, 547 (1973).
38. T. Giamarchi, *Quantum Physics in One Dimension* (DPMC, University of Geneva, 2003).

39. T. Zhang, M. Y. Sun, Z. Wang, W. Shi and P. Sheng, *Phys. Rev. B* **84**, 245449 (2011).
40. J. Gonzalez and E. Perfetto, *Phys. Rev. B* **72**, 205406 (2006).
41. D. Carpentier and E. Orignac, *Phys. Rev. B* **74**, 085409 (2006).
42. V. L. Ginzburg and L. D. Landau, *J. Exp. Theor. Phys.* **20**, 1064 (1950).
43. W. A. Little, *Phys. Rev.* **156**, 396 (1967).
44. J. S. Langer and V. Ambegaokar, *Phys. Rev.* **164**, 498 (1967).
45. D. E. McCumber and B. I. Halperin, *Phys. Rev. B* **1**, 1054 (1970).
46. T. Qian, W. Q. Ren and P. Sheng, *Phys. Rev. B* **72**, 014512 (2005).
47. M. Y. Sun, Z. L. Hou, T. Zhang, Z. Wang, W. Shi, R. Lortz and P. Sheng, submitted.
48. N. Metropolis, A. W. Rosenbluth, A. H. Teller and E. Teller, *J. Chem. Phys.* **21**, 1087 (1953).
49. B. Stoeckly and D. J. Scalapino, *Phys. Rev. B* **11**, 205 (1975).
50. D. J. Scalapino, Y. Imry and P. Pincus, *Phys. Rev. B* **11**, 2042 (1975).
51. C. Y. Qiu, T. Z. Qian and P. Sheng, *Phys. Rev. B* **75**, 024504 (2007).
52. K. Kobayashi and D. Stroud, *Physica C* **471**, 270 (2011).
53. H. J. Schulz, C. Bourbonnais, *Phys. Rev. B* **27**, 5856 (1983).
54. L. P. Gorkov, I. E. Dzyaloshinskii, *Zh. Eksp. Teor. Fiz.* **67**, 397 (1974).
55. R. A. Klemm, H. Gutfreund, *Phys. Rev. B* **14**, 1086 (1976).
56. P. A. Lee, T. M. Rice, R. A. Klemm, *Phys. Rev. B* **15**, 2984 (1977).
57. K. B. Efetov, A. I. Larkin, *Zh. Eksp. Teor. Fiz.* **66**, 2219 (1974).
58. M. Tinkham, *Introduction to Superconductivity*, 2nd ed. (MGH, New York, NY, 1996).
59. D. J. Scalapino, M. Sears and R. A. Ferrell, *Phys. Rev. B* **6**, 3409 (1972).
60. K. Y. Arutyunov, D. S. Golubev and A. D. Zaikin, *Phys. Rep.* **464,** 1 (2008).
61. U. Wolff, *Phys. Rev. Lett.* **62**, 361 (1989).
62. V. L. Berezinskii, *Sov. Phys. JETP* **32**, 493 (1971); **34**, 610 (1972).
63. J. M. Kosterlitz and D. J. Thouless, *J. Phys. C* **6**, 1181 (1973).